Characterizing the Nonlinear Behavior of Viscoelastic Materials: A Bayesian Approach Combining Oberst Beam Experiments and Digital-Twin Simulations

Kévin Jaboviste, Emeline Sadoulet-Reboul [ID], Rafael O. Teloli [ID], Gaël Chevallier [ID]

Université de Franche-Comté, SUPMICROTECH, CNRS, institut FEMTO-ST, F-25000 Besançon, France

corresponding authors: emeline.sadoulet-reboul@univ-fcomte.fr

Abstract

Viscoelastic materials are widely utilized in engineering for their advantageous damping properties, which enable effective energy dissipation. They are also valued for their stiffness properties, particularly in the case of suspension design. The behavior of these materials is complex, making it challenging to accurately incorporate them into simulations. If the dependence of dynamic properties on frequency and temperature has been commonly investigated, other phenomena still need to be studied, as for instance nonlinear phenomena leading to changes with the magnitude of stress/strain. Amongst them, the Payne effect, which manifests itself by a monotonous decrease of the storage modulus, remains difficult to integrate in the simulations, and is not often characterized experimentally for vibration purposes. An approach is proposed to identify the Payne effect by combining tests derived from the Oberst beam set-up and numerical simulations. To take into account the uncertainties inherent to the experiments, the identification process is based on a Bayesian identification framework which allows to determine the parameters and their statistical properties from a limited number of experimental measurements. The coupling between the Bayesian identification of dynamic properties of a polymer sample and a digital twin of the experimental set-up allows to identify the evolution of the storage modulus as a function of the strain amplitude, as well as the confidence interval around the mean value. The application on a silicone sample confirmed the decrease of the modulus with the strain level, with a good confidence level. The methodology developed here for the specific case of the Payne effect can be extended more generally to the experimental characterisation of nonlinear behavior.

Keywords: Nonlinear viscoelasticity, Oberst, Bayesian identification, Digital Twin

1. Introduction

Viscoelastic materials are commonly recognized as efficient passive damping systems, and are widely used in engineering fields with applications ranging from automotive exhaust systems and aircraft fuselages to bio-inspired devices [1, 2]. The viscoelastic behavior can be described by the relaxation or creep functions that express the delay between the applied force and the displacement. The tunable mechanical properties depend on several aspects such as the frequency range, the temperature, the preload and the strain field. This work focuses on the amplitude-dependence of viscoelastic materials, especially strong in polymeric materials containing fillers, e.g. carbon black fillers.

The amplitude-dependence behavior of filled polymers is led by nonlinear mechanical features, such as hysteresis and stress softening (Mullins effect [3]). Among these, the Payne effect [4] (also known as Fletcher-Gent effect [5]) stands out due to its influence on the strain-dependent storage modulus of reinforced polymers, accounting for the decrease in storage modulus as a function of the strain rate and persists through cycles. There

is an industrial interest in characterizing the Payne effect, since the most pronounced variations in mechanical properties due to this phenomenon occur within a strain range commonly experienced by engineering devices (0.1 to 50% strain [6], [7]), such as stabilization solutions for optical instruments. The origin of the Payne effect is not clearly defined - it depends on filler-matrix interactions and changes in the micro-structure of the material [8, 9]-, but it is a reversible phenomenon achieved by a continuous breaking and reforming Van-der-Walls forces between carbon black particles [10].

The viscoelastic behaviour can be characterised experimentally using different approaches, which can be classified as quasi-static or Dynamic Mechanical Analyzer tests, measurements on a viscoanalyser, and dynamic tests. The technique of Dynamical Mechanical Analysis (DMA) is used in [11] to investigate the nonlinear behavior of a viscoelastic material, and in [12, 13, 14] to investigate the Payne effect in viscoelastic materials. Jrad and al. [14] conducted DMA tests in order to identify parameters of a nonlinear Generalized Maxwell Model and exhibited the Payne effect. Rendek and Lion [12] performed a quasi-static harmonic tension test on filled-reinforced rubbers by gradually changing the strain amplitude, rendering it possible to capture the softening of the material in the time domain - tests ranged from 0.2% to 13% of strain amplitude. Although Rendek and Lion achieved to reach different strain amplitude levels, experimental tests demanded a very high execution time. Luo and al. [13], in turn, employed the DMA procedure to characterize the dependence of mechanical properties on frequencies and strain amplitudes, with emphasis on the Krauss model that was used to capture the Payne effect. To impose larger strain amplitudes than are possible in the viscoanalyser, facilitating then the visualization of the amplitude dependency, Luo and al. stretched the specimens under a prestrain of 10%. A viscoanalyzer based on the shear mode has been developed in [15] to characterize the shear stiffness of preloaded viscoelastic materials between 200 and 3500 Hz and without using frequency-temperature equivalences and shifting the measurements to higher frequencies as commonly done with DMA measurements. Although the device has been applied to studies of linear viscoelasticity, to the best of the authors' knowledge it has not given rise to applications in nonlinear viscoelasticity. Finally, METRAVIB has developed a commercial DMA test machine (VHF104) for high frequency testing under sinusoidal excitation up to 10 kHz and for strain up to 30 % : Syed et al. [16] conducted such high-frequency DMA tests to reconstruct the frequency response curves of polymer-filled samples, and then extract the nonlinear strain dependence in the vicinity of resonance frequencies. The evolution of the storage modulus as a function of strain amplitudes, however, has not been traced. The device seems to suffer from a lack of accuracy in capturing and monitoring the strain range as mentioned in [17] with the proposal of a new High Frequency Dynamic Mechanical Analysis (HFDMA) test system. From this overview of some applications involving DMA tests to characterize the Payne effect, note that restrictions on the experimental setups (test machines and sample holder) exist, either in achieving amplitudes that highlight the strain-dependent storage modulus, or by the time required to perform these tests. Another experimental procedure to characterize the vibratory behavior of polymers is the ASTM E-756 Vibrating Beam Technique applied to the modified Oberst beam configuration [18, 19]. Simply put, the (modified) Oberst beam consists of a multi-layer cantilever beam - the test sample is glued between aluminum or steel sheets, resulting in a sandwich configuration. Based on input and output data, the differences between the Frequency Response Functions (FRFs) of the sandwich structure and a uniform one are compared to retrieve the storage modulus and the loss factor of the polymeric sample. This approach only allows the identification of these mechanical parameters in the vicinity of resonance frequencies, an important drawback of the methodology. Nevertheless, several ways exist to expand the characterization range of the parameters, either by adjusting the excitation

conditions [20], or by changing the configuration of the layers [21]. Recent contributions in the literature also suggest the use of the Oberst beam method for inferring characteristics in vibration damping of reinforced polymers [22, 23, 24].

This paper proposes to use a modified Oberst beam technique to experimentally characterize the nonlinear behavior of viscoelastic material, and in particular the evolution of the storage modulus as a function of the strain amplitude obtained from vibration data of free response system. The reconstruction of these mechanical properties is done by capturing the resonance frequency and damping parameters that evolve nonlinearly depending on the response amplitude - a feature of the Payne's effect. To the best of our knowledge, this is the first contribution that exploits the Oberst beam to characterize the nonlinear dependency of storage modulus on strain amplitudes due to the Payne effect.

In this work, the first bending mode of the Oberst beam is at the center of the analysis, since it is responsible for the largest strain amplitudes on the polymeric specimen. To track the nonlinear evolution of resonance decay responses data, the sliding least-squares method is considered. The key idea is to measure the backbone curves from free responses and thereafter relate these to a stochastic parametric model. Similar approaches to the one adopted are reported in experimental applications involving vibration absorbers [25, 26], mechanical systems with geometric nonlinearities [27], and assembled structures [28, 29, 30]. When considering the Oberst beam, however, estimating backbone curves from resonance decay responses with nonlinear parametric approximations lack contributions.

Toward this background, the identification scheme here proposed to obtain the storage modulus as function of strain amplitudes includes, firstly, the estimation of the instantaneous resonant frequency and the damping for free responses measured from independent experimental realizations. A stochastic model is put forward to reconstruct the backbone curves and then the Markov-Chain Monte Carlo algorithm is used to update the probability density functions of each random variable based on the Bayesian inference. This step in the identification procedure is done to ensure that the model takes into account uncertainties in the experimental data related to the variability of the measurement process. Bearing mind that the strain on the polymeric material cannot be directly measured during vibration tests, a digital-twin formulated as a 2D finite element model of the Oberst beam is proposed to infer information about the mechanical properties of the material. Apart from being useful for experiment design, the digital twin is the main modification to the original Oberst beam technique, since it is no longer necessary to use a uniform beam. Having numerical data cross-correlated with experimental measurements, uncertainties are propagated on the storage modulus and the Payne effect is characterized with probabilistic confidence intervals.

For covering all these steps, the work is divided as follows: section 2 introduces the Oberst Beam, the experimental setup, and the sliding least-squares method to obtain the free responses of the structure. Section 3 is dedicated to describing the identification methodology. Next, section 4 presents an application of the identification framework to a numerical case, where the frequency and damping backbones of a nonlinear oscillator are extracted from free responses. The application to the experimental case of the Oberst beam is described in section 5. This section presents the stochastic models derived from the Bayesian approach adopted for the backbone identification problem. Section 6 introduces the digital-twin of the Oberst beam and discusses the presence of the Payne effect on the polymeric specimen. Concluding remarks and trends for future research are presented in section 7.

2. Oberst Beam Experimental Technique

2.1. Experimental setup

The Oberst beam consists of a base beam that provides the necessary stiffness, associated to a damping layer. Fig. 1(a) presents the configuration used for the experiments, with the presence of the SI965 silicone sample glued between two metallic skins. The beam is a sandwich structure with two stainless steel plates of length 0.146 m, width 0.03 m, and thickness 0.001 m, the polymer sample is glued at one end and has dimensions 0.05 m×0.03 m×0.0025 m. The beam is clamped at the other end and subjected to free vibrations: an initial displacement is applied at the free end using a nylon wire of negligible mass, a set of standard masses consisting in cylindrical weights between 0.5 kg and 1 kg, and a pulley (Fig. 1 (b)). The wire is cut and the free vibratory response is recorded by an accelerometer. Fig. 2 shows a raw acceleration measurement: the free oscillatory motion mainly corresponds to the first bending mode, whereas the amplitude of this movement decreases slowly until the system reaches its final equilibrium state.
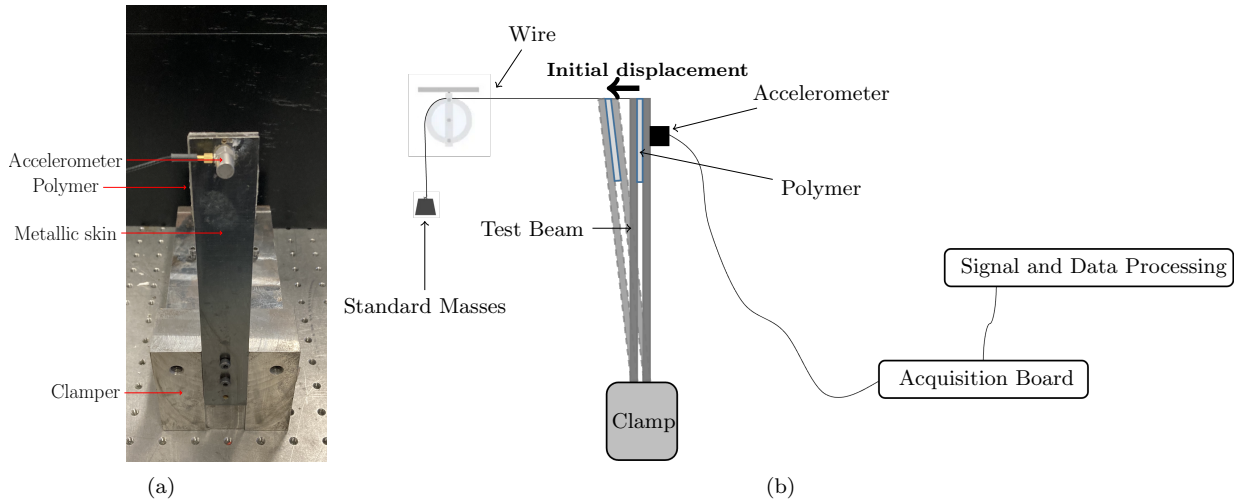

(a) (b)

Fig. 1: Experimental set-up used for the Payne effect characterization : (a) Oberst beam and the experimental apparatus, (b) Schematic representation of the methodology used to obtain the free responses.
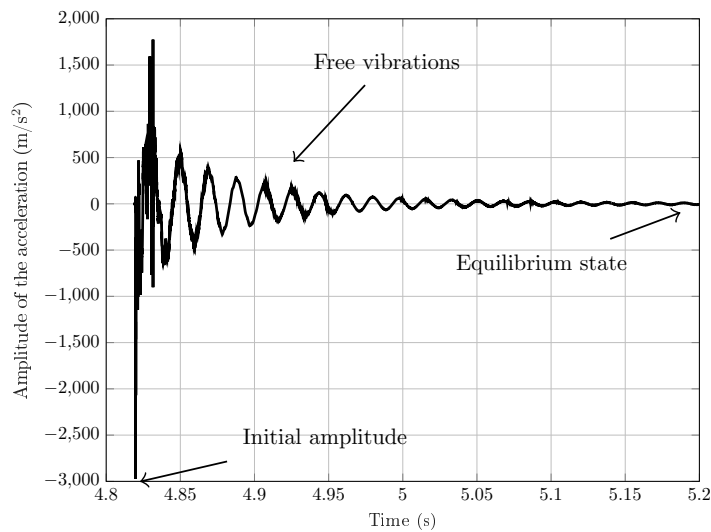

Fig. 2: Example of a raw acceleration signal.

2.2. Identification of the instantaneous damping and frequency

The acceleration signal is post-processed to identify the dynamic properties of the structure. The whole process for identification is detailed in Appendix A. After post-processing of the measured data, the instantaneous evolution of damping and frequency is estimated using the sliding least-squares method and minimizing the objective function F_{obj},

$$F_{obj} = \min_{\omega_0, \xi} \sum_{i=1}^{n} \left(q(t_i; \xi, \omega_0) - q_{exp}(t_i) \right)^2, \tag{1}$$

where $q(t_i; \xi, \omega_0)$ represents the analytical form of the displacement given in Appendix A Eq.A.2 and it is written as function of instantaneous damping ξ and frequency ω_0; t_i denote the time steps included in the period $[t; t + dt]$ that composes the sliding window; q_{exp} represents the experimental displacement extracted from the oscillatory response.

Fig. 3 presents the evolution of the instantaneous frequency and damping for the Oberst beam. Edge effects can be observed due to the least-squares method, but the identified signals contain enough information for a large post-processing. The results confirm the softening dynamic behavior of the structure as a function of the displacement amplitude. This phenomenon is due to the Payne effect linked to the presence of the charged silicone sample $SI965$. Because of it, the dynamic behavior of the beam depends on the strain rate of the polymer. Section 6 discusses in detail the characterization of the Payne effect as function of the strain rate of the polymeric sample.
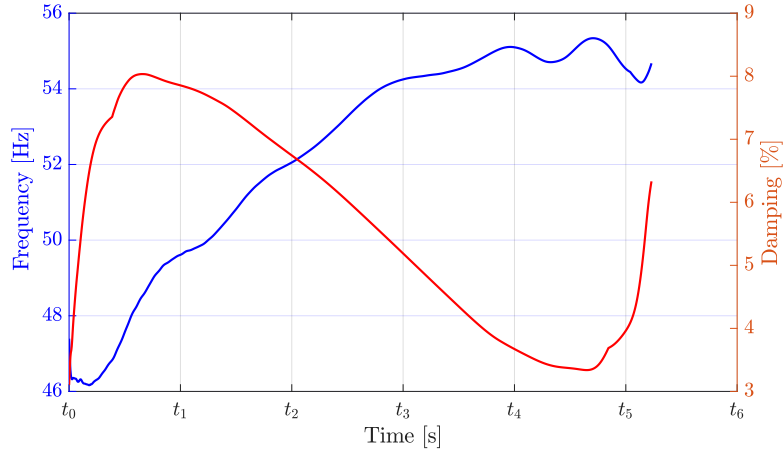

Fig. 3: Evolution of the identified instantaneous frequency and damping for the first mode of the Oberst beam

3. Bayesian Model Identification

The primary objective of this section is to establish a versatile framework for characterizing viscoelastic materials using the modified Oberst beam technique. This approach allows for broader applicability, extending its utility even to scenarios involving more complex material laws. The identification framework encompasses three crucial steps: *model selection*, *sensitivity analysis*, and *Bayesian parameter updating*. Initially, the focus lies on identifying models capable of effectively describing the relevant quantities extracted from experimental responses. These numerical models serve as a means to establish the relationship between these variables and the mechanical properties of the elastomer, as well as the deformation amplitude. Once appropriate candidate models have been selected, the subsequent step involves assessing the influence of their parameters on the overall outputs. This is achieved through sensitivity analysis, utilizing Sobol indices. The objective of this

analysis is to narrow down the design space and facilitate subsequent uncertainty quantification, particularly in the context of inverse assessment involving model and parameter uncertainties. Lastly, the parameter updating problem is addressed within the Bayesian framework. This comprehensive approach to the identification scheme
155 is thoroughly discussed and examined throughout this section.

3.1. Model selection

Since the instantaneous variations of the parameters of interest are extracted from the free response for different ranges of initial conditions, the work focuses on identifying mathematical models and their respective parameters that are able to represent relevant physical aspects observed experimentally. This identification
160 process could be summarized as a classical data-driven regression problem, where a nonlinear basis functions is proposed and the parameter estimation is obtained by the classical least-squares method, as performed by [27]. However, in this work, the nonlinear basis for describing frequency and damping as a function of displacement - the so-called backbone curves - is assumed to be unknown, and as alternative, the strategy chosen here is to adopt a set of candidate nonlinear functions. Without loss of generality, consider the following regression
165 problem:

$$\boldsymbol{y} = \boldsymbol{\Theta}\mathcal{X} + \boldsymbol{\varepsilon} \tag{2}$$

where $\boldsymbol{y} \in \mathbb{R}^N$ is a vector containing the quantity of interest, $\mathcal{X} \in \mathbb{R}^{N \times p}$ represents the design matrix of arbitrary nonlinear basis functions which are responsible for transforming an input (in this work, the input is considered as the envelope of the displacement $\mathcal{Q}(t) \in \mathbb{R}^N$), and $\Theta \in \mathbb{R}^p$ is formed by coefficients corresponding to each nonlinearity; $\boldsymbol{\varepsilon} \in \mathbb{R}^N$ represents the inherent randomness in the noisy observations. For the problems
170 here addressed, there are more data samples than candidate functions, thus $N \gg p$.

To make the regression problem presented in Eq. (2) valid for estimating the damping and instantaneous frequency, the hypothesis assumed is that the backbone curves, which give insight into the nonlinear behavior of dynamical systems, can be adequately approximated by the decaying envelope of the system.

Note that $\mathcal{X}$ can be constructed from a wide candidate space, ranging from polynomial functions to trigono-
175 metric ones [31]. If this problem is treated in a classical regression framework, the coefficients corresponding to each nonlinear term in the candidate library will have a non-zero contribution to the approximation. This approach can lead to a number of drawbacks in the identification process, such as inclusion of terms that do not necessarily represent observations seen experimentally; render the parameter estimation procedure numerically unstable for a large set of candidates; cause model overfitting. For equation discovery in the context of nonlinear
180 dynamical systems, the alternative that has recently been evoked in the literature lies in using the sparse regression algorithm [31] and different variations of the same approach [32, 33]. Also noteworthy is the least absolute shrinkage and selection operator (LASSO) method, which introduces regularization by incorporating a penalty term into the regression equation [34]. In these methodologies, the primary objective remains consistent: to induce sparsity over the parameter vector Θ, resulting in only a few non-zero terms, but capable to define the
185 relevant physics. The efficiency of these methods depends directly on the proper choice of the hyperparameters that are responsible for the sparsity.

With respect to the mentioned works, this paper considers a simpler and still effective way to deal with the regression problem. Consider the following candidate basis vector constructed on a polynomial form to

represent the quantity of interest $\boldsymbol{y}$:

$$\mathcal{P}(\mathcal{Q}) = \begin{bmatrix} \mathcal{Q}^0(t) & \mathcal{Q}^1(t) & \cdots & \mathcal{Q}^n(t) \end{bmatrix}, \tag{3}$$

for the candidate basis $\mathcal{P}(\mathcal{Q})$, $\mathcal{X}$ is constructed for all possible combinations of the candidates space. Thus, the estimation of the coefficients is performed using the classical least-squares method:

$$\hat{\boldsymbol{\Theta}} = \left(\mathcal{X}^T \mathcal{X} \right)^{-1} \mathcal{X}^T \boldsymbol{y}, \tag{4}$$

where $\hat{\boldsymbol{\Theta}}$ denotes the deterministic estimation of model parameters. To assist in the process of selecting the model that best fits the experimental data while avoiding overparametrization, two statistical tools commonly used in data-driven modeling are employed. The first is the $k-$fold cross-validation (CV), which consists of randomly dividing the data into k sets, such that $k-1$ subsamples are used for training and the k left is used for validation. This process is repeated k times until all data have been equally used for training and validation. At the end, the mean-square error (MSE) between each model and the experimental data is estimated considering only the validation folds.

Having the MSE, the Akaike information criterion (AIC) is then used to verify which model offers the best trade-off between the fit score and complexity, thus reducing the overparameterization risk.

Sensitivity Analysis

After appropriate model selection, the sensitivity analysis is put forward to quantify the influence that coefficients have on the output. Those whose variability results in relatively small influence on the predictive ability of the model are considered as determined quantities, and their values are assigned based on the deterministic estimation conducted by the least-squares method. The global sensitivity analysis is carried out by means of the Sobol indices that are, in turn, calculated by the Polynomial-Chaos Expansion (PCE). The procedure is performed with UQLab framework [35], and further details of the methodology are available in [36].

Once this study is realized, it then becomes possible to perform the Bayesian inference, where the remaining model coefficients are calibrated to increase the predictive ability to forecast the relevant physical behavior of the real system in the presence of data uncertainties. This approach renders the model stochastic.

Bayesian inference framework

Bayesian inference is used in this work to increase the statistical information about the system response based on prior knowledge. The model coefficients $\boldsymbol{\Theta}$ are assumed to be random variables, and the experimental observations $\mathcal{D} \equiv \boldsymbol{y}$ are also random. Thus, considering that fluctuations in the system's response are related to the measurement process, the Eq. (2) is described as:

$$\mathcal{D} = \mathcal{D}^{\mathcal{M}}(\boldsymbol{\Theta}) + \boldsymbol{\varepsilon}, \tag{5}$$

where $\mathcal{D}^{\mathcal{M}}(\boldsymbol{\Theta})$ corresponds to the model predictions given a set of parameters $\boldsymbol{\Theta}$, and $\boldsymbol{\varepsilon} \sim \mathcal{N}(\boldsymbol{0}, I\sigma_{\varepsilon}^2)$ is a random noise vector $\boldsymbol{\varepsilon} \in \mathbb{R}^N$ with covariance $I\sigma_{\varepsilon}^2$, where I is the identity matrix, i.e., it is assumed an additive decorrelated Gaussian noise.

Considering unknown variance σ_ε^2 and model parameters $\boldsymbol{\Theta}$, a prior probability density function (PDF) $\pi(\boldsymbol{\Theta}, \sigma_\varepsilon^2)$ is assigned to the random vectors considering only the knowledge degree about $\boldsymbol{\Theta}$ and σ_ε^2 before new evidences. The Bayesian framework is then used to update the prior PDF of the numerical model parameters based on the data from the system of interest. The Bayes' rule of conditional probability to infer the posterior PDF is given by:

$$\pi(\boldsymbol{\Theta}, \sigma_\varepsilon^2 | \mathcal{D}) = \frac{\pi(\mathcal{D} | \boldsymbol{\Theta}, \sigma_\varepsilon^2) \pi(\boldsymbol{\Theta}, \sigma_\varepsilon^2)}{\pi(\mathcal{D})}, \tag{6}$$

where $\pi(\boldsymbol{\Theta}, \sigma_\varepsilon^2 | \mathcal{D})$ is the updated posterior probability given the system observations $\mathcal{D}$, $\pi(\mathcal{D} | \boldsymbol{\Theta})$ is the likelihood function, $\pi(\boldsymbol{\Theta}, \sigma_\varepsilon^2)$ is the prior probability density function containing knowledge for candidate model parameters, and the error variance. Note that the initial information that constitutes the prior PDF is given by the deterministic values $\hat{\boldsymbol{\Theta}}$ found during the model selection step. In addition, considerations are made: the term $\pi(\mathcal{D})$ is a normalizing constant that ensures $\pi(\boldsymbol{\Theta}, \sigma_\varepsilon^2 | \mathcal{D})$ as a probability density function with integral equal to unity; $\pi(\boldsymbol{\Theta}, \sigma_\varepsilon^2)$ follows a non-informative Uniform distribution $\pi(\boldsymbol{\Theta}, \sigma_\varepsilon^2) \sim \mathcal{U}\big((1 - \Delta)\{\hat{\boldsymbol{\Theta}}, \sigma_\varepsilon^2\}^T, (1 + \Delta)\{\hat{\boldsymbol{\Theta}}, \sigma_\varepsilon^2\}^T\big)$. In this scenario, Eq. (6) is simplified into $\pi(\boldsymbol{\Theta}, \sigma_\varepsilon^2 | \mathcal{D}) \propto \pi(\mathcal{D} | \boldsymbol{\Theta}, \sigma_\varepsilon^2)$, i.e., the updated posterior PDF is proportional to the likelihood distribution.

With this in mind, efforts to determine the posterior distribution concentrate on estimating the likelihood function. Thus, based on Eq. (5) and the assumptions outlined above, its analytical expression is defined as:

$$\pi(\mathcal{D} | \boldsymbol{\Theta}, \sigma_\varepsilon^2) \propto \exp\left(-\frac{1}{2} \frac{\left(\mathcal{D} - \mathcal{D}^{\mathcal{M}}(\boldsymbol{\Theta})\right)^T \left(\mathcal{D} - \mathcal{D}^{\mathcal{M}}(\boldsymbol{\Theta})\right)}{\sigma_\varepsilon^2}\right). \tag{7}$$

The Bayesian framework provides all the theoretical elements needed to evaluate the likelihood function. This task can become non-trivial, especially when a combination of parameters with different distributions are sampled simultaneously. In this work, we adopted the strategy of sampling the posterior function numerically by means of the Markov Chain Monte Carlo (MCMC)/Metropolis-Hastings algorithm which is a popular method which could be applied for complex models without analytically tractable posterior distribution. However, it is interesting to note that analytical solutions exist for the case studied here. They are presented in the appendix Appendix B to confirm the validity of the results obtained by MCMC. The random variables $\boldsymbol{\Theta}$ and σ_ε^2 are limited to the interval $[\{\boldsymbol{\Theta}_{\min}, (\sigma_\varepsilon^2)_{\min}\}^T, \{\boldsymbol{\Theta}_{\max}, (\sigma_\varepsilon^2)_{\max}\}^T]$, whose current state is symmetrically normalized as $\boldsymbol{\Theta}' = (1 - \boldsymbol{x})\boldsymbol{\Theta}_{\min} + \boldsymbol{x}\boldsymbol{\Theta}_{\max}$ and $(\sigma_\varepsilon^2)' = (1 - \boldsymbol{x})(\sigma_\varepsilon^2)_{\min} + \boldsymbol{x}(\sigma_\varepsilon^2)_{\max}$; $\boldsymbol{x}$ is a random variable $\in [0, 1]$ that represents generated candidates for the posterior distribution. These candidates are sampled from a normal distribution with standard deviation σ_p, such that this hyperparameter is adjusted to obtain an acceptance rate of candidates $40 \sim 50$ %. Only 90% of the Monte Carlo simulations n_s are considered in the final stationary Markov chain (burn-in of 10%).

4. Numerical Application

Before proceeding with the proposed methodology on experimental data, this section is dedicated to illustrate the main aspects discussed up to this point in a numerical application. In particular, focus will be given to the applicability of the sliding least-squares method for extracting instantaneous frequency and damping, and the model selection procedure. Since this is only a numerical application, the sensitivity analysis and Bayesian inference steps will be covered directly on the experimental application of the Oberst beam.

The motion equation of the nonlinear system examined here is given by:

$$m\ddot{q}(t) + c_1\dot{q}(t) + k_1 q(t) + c_2|\dot{q}(t)|\dot{q}(t) + k_3 q^3(t) = f(t) \tag{8}$$

where m [kg] is the mass, c_1 [Ns/m] is the viscous damping, k_1 [N/m] is the linear stiffness, c_2 [Ns^2/m^2] is the quadratic damping coefficient and k_3 [N/m^3] is the cubic stiffness. Overdots represent displacement differentiation with respect to time, and $f(t)$ is an applied force. Table 1 presents the numerical values of the coefficients used for this application. To better emulate a real application, it was added to the system response, in all simulated situations, a Gaussian noise to have a signal to noise ratio (SNR) of 40 dB.

Table 1: Nonlinear system parameters.

m [kg]	c_1 [Ns/m]	k_1 [N/m]	c_2 [Ns^2/m^2]	k_3 [N/m^3]
1.5	4	6×10^3	10	1×10^7

When a large initial vibration amplitude is applied, the free response decays and the vibration regime follows the backbone curve [37, 25]. This is the reason behind the approach adopted by this paper, dealing directly with the backbone curves instead of investigating the analytical solution of the free response to estimate the system parameters. For deriving the analytical expressions of the backbone curves, the Harmonic Balance method [38] is applied on Eq. (8). Considering a harmonic force $f(t) = F\sin(\omega_0 t - \phi)$ and the first-order approximation of the system's response lead to:

$$\omega_0^2 = \frac{k_1}{m} + \frac{3}{4}\frac{k_3}{m}\mathcal{Q}^2(t) \quad \Rightarrow \quad \omega_0^2 = \omega_n^2 + \alpha\mathcal{Q}^2(t), \tag{9}$$

where $\omega_n = \sqrt{k_1/m}$ is the natural frequency when considering the linear system, and

$$\xi = \frac{c_1}{2m\omega_0} + \frac{8}{3}\frac{c_2\omega_n}{\pi m\omega_0}\mathcal{Q}(t) \quad \Rightarrow \quad \xi = \xi_0(\omega_0) + \lambda(\omega_0)\mathcal{Q}(t). \tag{10}$$

Note that both expressions, Eqs. (9)-(10), are rewritten in the form of a regression problem, where α and λ are coefficients related to frequency and damping, respectively. Therefore, for the nonlinearity investigated in this numerical application, the frequency can be obtained directly from the measured response envelope of the system under analysis, without interference or participation of damping. On the other hand, in order to estimate the damping, it is necessary to take into account the frequency dependency.

The free response of the system described by Eq. (8) was obtained considering different initial conditions and $f(t) = 0$, from 0.5 to 10 mm sampled every 0.5 mm. The Newmark method is used to time integrate the motion equation, considering a sampling frequency of 4096 Hz. Fig. 4 illustrates an observation of the acceleration obtained from the system for an initial condition of 10 mm. From this raw acceleration signal, the sliding least-squares algorithm (see Appendix A) is applied.

Fig. 5 depicts the displacement obtained by the numerical integration scheme applied on the acceleration data from Fig. 4. To obtain this curve, the DC term was removed. Nevertheless, there was no need to apply the EMD method, since the data observed in this section only concern the single-degree-of-freedom nonlinear oscillator. In addition to the displacement, the figure also shows the reconstructed displacement, as well as the response envelope that will later be used to build the backbone curves. Note that this figure only illustrates
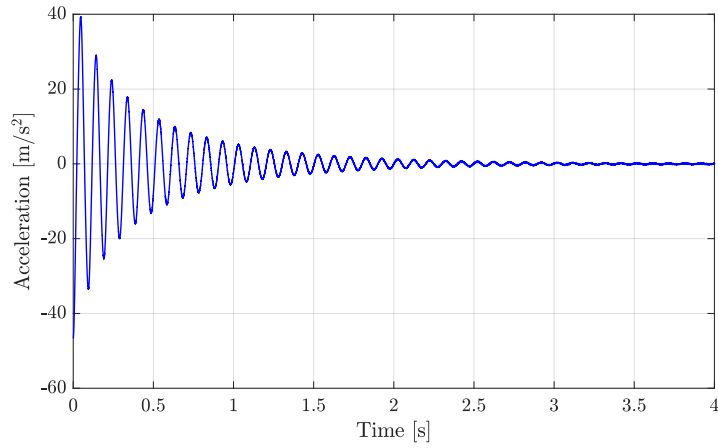
9

Fig. 4: Acceleration response obtained through numerical integration of the equation of motion (8).

the results for an initial condition of 10 mm. For the model selection and parameter calibration step, all data generated for the 20 initial conditions will be used, even if for small displacements the system presents linear behavior, i.e., nonlinearity is not activated. This strategy was adopted because, in a real application case, it is not possible to know exactly from which initial condition the system will exhibit nonlinear behavior - therefore, all conditions must be used during identification to ensure that no information is lost.
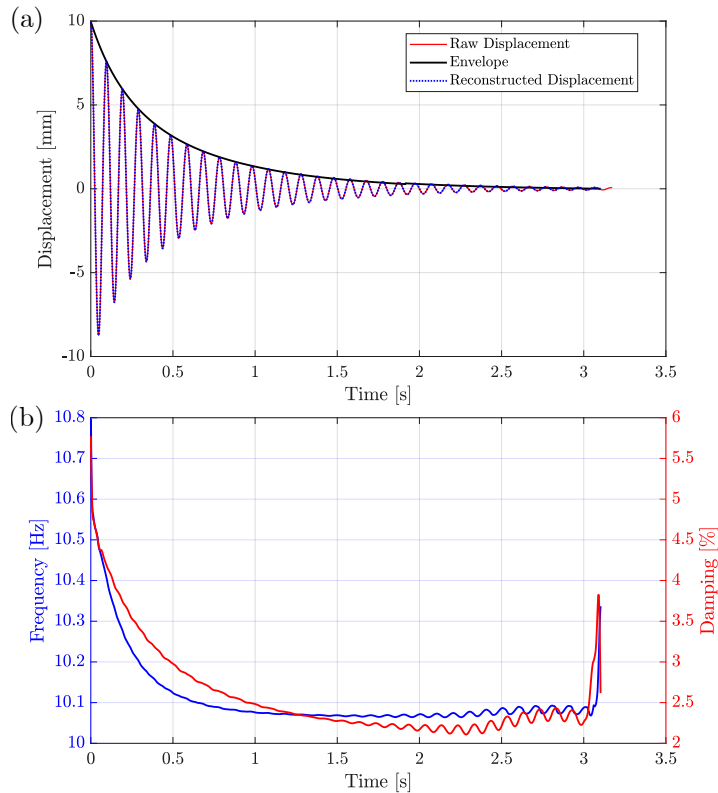

Fig. 5: Data extraction performed by the sliding least-squares method applied on the nonlinear numerical model. Top figure: ⎯⎯ is the response envelope, ⎯⎯ is the noisy raw displacement and −− represents the reconstructed displacement. Bottom figure: ⎯⎯ is the instantaneous frequency, whereas ⎯⎯ represents the damping.

Fig. 5 (b) shows the variations of the instantaneous frequency and damping as a function of time obtained using the sliding least-squares method. One can observe the hardening effect in the frequency plot as a result of the nonlinear stiffness term, marked by an increase in the system frequency for large displacement amplitudes. A similar increase in damping behavior can also be noted. Worthy of note the sudden drop of these values in the very first instants of time. During these first instants, the displacement amplitude drops very quickly as

10

the level of damping in the polymer is high (a few %). The high displacements are reached for each test before the end of the first period, such that the identification methodology based on a window representing a period does not allow capturing them. Thus, even adjusting the size of the sliding window, the high damping of the system causes edge effects to exist on the extracted quantities. Similar effects are also found when the Hilbert transform is used to analyze the free vibration of systems that have high damping values [39].

As the free response fades away, notably from the 1.5 second time instant on, these quantities of interest begin to show pronounced noise in their estimates. To reduce the influence of these deviations on the identification process, only the initial 50% of all available samples are considered.

Once the entire data post-processing is completed, the model selection step is carried out. The following polynomial basis is considered as candidate to generate models for both, damping and frequency:

$$\mathcal{P}(\mathcal{Q}) = \begin{bmatrix} \mathcal{Q}^0(t) & \mathcal{Q}^{1/3}(t) & \mathcal{Q}^{2/3}(t) & \mathcal{Q}^1(t) & \mathcal{Q}^{4/3}(t) & \mathcal{Q}^{5/3}(t) & \mathcal{Q}^2(t) \end{bmatrix}, \tag{11}$$

such that the models of the variables of interest considering all possible terms, i.e. $\mathcal{X} = \mathcal{P}(\mathcal{Q})$, are given by:

$$\boldsymbol{\omega}_0 = \underbrace{\begin{bmatrix} \omega_{n_f} & \delta_f & \beta_f & \lambda_f & \kappa_f & \gamma_f & \alpha_f \end{bmatrix}}_{=\boldsymbol{\Theta}_f} \mathcal{X} \tag{12}$$

$$\boldsymbol{\xi} = \underbrace{\begin{bmatrix} \xi_{0_d}(\omega_0) & \delta_d(\omega_0) & \beta_d(\omega_0) & \lambda_d(\omega_0) & \kappa_d(\omega_0) & \gamma_d(\omega_0) & \alpha_d(\omega_0) \end{bmatrix}}_{=\boldsymbol{\Theta}_d} \mathcal{X}, \tag{13}$$

where $\boldsymbol{\Theta}_f$ and $\boldsymbol{\Theta}_d$ correspond to the frequency and damping coefficients, respectively. As previously mentioned, the goal of the model selection step is to test all possible parameter combinations, and in the end, to determine which model is most cost-effective between fit value and complexity. For this, five-fold CV strategy was used, i.e. 16 free response data were randomly used for training and the remaining 4 for validation - the procedure was performed 5 times such that all data were used for training and validation.

Table 2 presents the three models that showed the best AIC metric values for the regression on the instantaneous frequency values. Note that the best model obtained by the selection algorithm, i.e. the one with the lowest AIC value, is in fact equal to the model described in Eq. (9). The values of the coefficients obtained by the regression method are $\omega_{n_f}^2 = 4000$ rad^2/s^2 and $\alpha_f = 4.85 \times 10^6$ N/(m^{3}kg), whereas the analytical values are $\omega_n^2 = 4000$ rad^2/s^2 and $\alpha = 5 \times 10^6$ N/(m^{3}kg), which represents a difference of $\sim 3\%$ over the value obtained for the nonlinear coefficient. Fig. 6 shows a comparison between the identified frequency backbone curve, the analytical one, as well as the extracted backbone for an initial condition of 10 mm. The identified frequency backbone is able to reproduce, with good accuracy, the curve extracted by the sliding least-squares method, except for amplitude values close to 10 mm, which is expected due to the presence of edge effects.

Table 2: Models obtained for regression on the instantaneous frequency (numerical application) and their respective AIC values.

Model	AIC
$\omega_0^2 = \omega_{n_f}^2 + \alpha_f \mathcal{Q}^2(t)$	25.51
$\omega_0^2 = \omega_{n_f}^2 + \beta_f \mathcal{Q}^{2/3}(t) + \alpha_f \mathcal{Q}^2(t)$	33.45
$\omega_0^2 = \omega_{n_f}^2 + \delta_f \mathcal{Q}^{1/3}(t) + \alpha_f \mathcal{Q}^2(t)$	33.50

Once the model identification for instantaneous frequency has been conducted, it is now possible to perform the regression for damping. Table 3 presents the three models that showed the best AIC metric values for the
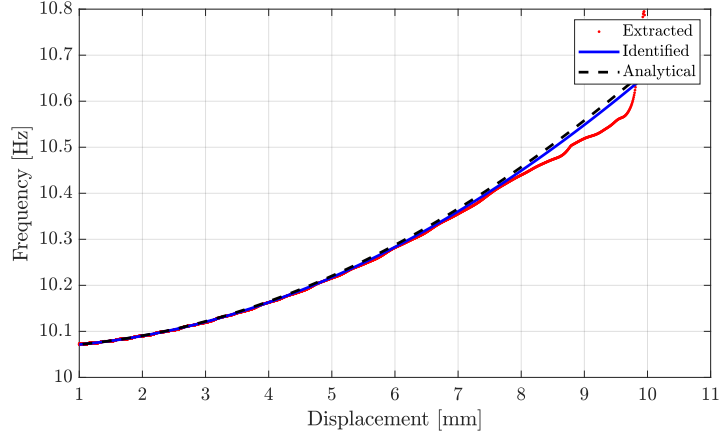
Fig. 6: Comparison of the identified frequency backbone with respect to the curve extracted by the sliding least-squares method.

regression on the damping values. Again, the model found that best represents the available data corresponds to the analytical damping model presented in Eq. (10). The values of the estimated coefficients without the normalization by the ω_0 term are $\xi_{0_d} = 1.31$ and $\lambda_d = 184.41$, whereas the analytical values are $\xi_0 = 1.33$ and $\lambda = 178.95$, which represents a difference of $\sim 3.6\%$ over the value obtained for the nonlinear coefficient. The comparison between the damping backbone identified, the analytical response and the curve extracted by the sliding least-squares method is shown in Fig. 3. The results obtained indicate that the damping model is able to represent the numerical values in good agreement, except in the region around 10 mm, again due to the presence of the edge effects mentioned earlier.

Table 3: Models obtained for regression on damping (numerical application) and their respective AIC values.

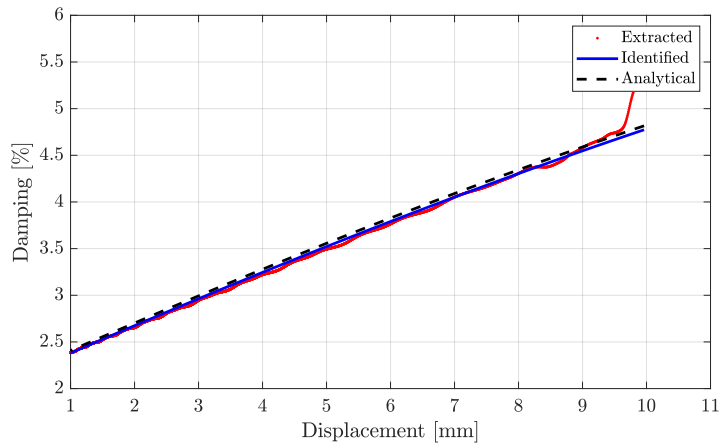| Model	AIC
$\xi = \xi_{0_d}(\omega_0) + \lambda_d(\omega_0)\mathcal{Q}(t)$	212.11
$\xi = \xi_{0_d}(\omega_0) + \lambda_d(\omega_0)\mathcal{Q}(t) + \kappa_d(\omega_0)\mathcal{Q}^{4/3}(t)$	216.24
$\xi = \xi_{0_d}(\omega_0) + \lambda_d(\omega_0)\mathcal{Q}(t) + \alpha_d(\omega_0)\mathcal{Q}^2(t)$	216.82

Fig. 7: Comparison of the identified damping backbone with respect to the curve extracted by the sliding least-squares method.

Overall, the results discussed throughout this section indicate that the proposed methodology is capable of handling the estimation of the damping and instantaneous frequency backbone curves from the free response of a nonlinear system. The next section deals with assessing the feasibility of the identification algorithm on an experimental application.

5. On the Stochastic Parameter Calibration of the Oberst Beam

5.1. Frequency backbone calibration

Since the free response data acquired from the Oberst beam were previously presented during section 2, this section is entirely devoted to the model calibration procedure for instantaneous frequency and damping variables. Fig. 8 illustrates the free displacement response of the beam for an initial amplitude of 8.5 mm, as well as the reconstructed output and its envelope. To minimize the importance of edge effects on the identification methodology, only the first 80% of the time response is considered. A total of 20 experimental responses were obtained from the Oberst beam with initial conditions ranging from 1 to 8.5 mm.
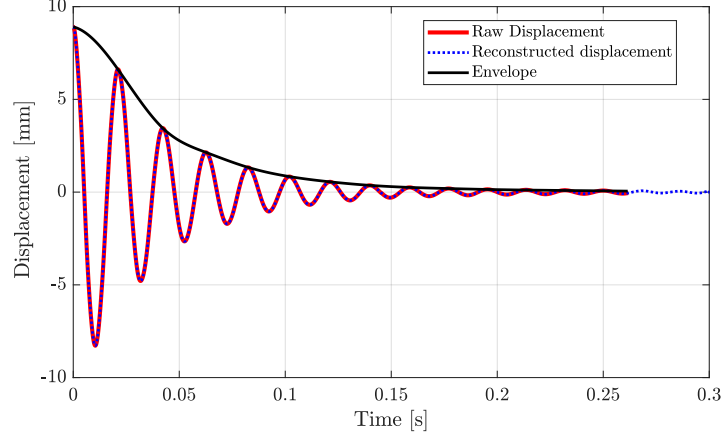

Fig. 8: Data extraction performed by the sliding least-squares method applied on the Oberst beam. This free response is obtained for an initial condition of 8.5 mm.

The polynomial basis used for the experimental application is the same as described by Eq. (11). As with the numerical application, the 5-fold CV strategy was used. In this context, Table. 4 presents the three frequency regression models that have the best performance on the AIC values. Note that the model that shows satisfactory predictive ability for the frequency data is the one that contains the fewest terms, $\omega_0^2 = \omega_{n_f}^2 + \delta_f \mathcal{Q}^{1/3}(t)$. Thus, this is the model chosen to proceed with the calibration procedure on its parameters.

Table 4: Models obtained after regression on instantaneous frequency data (experimental measurements) and their respective AIC values.

Model		AIC
$\mathcal{M}_1^f:$	$\omega_0^2 = \omega_{n_f}^2 + \delta_f \mathcal{Q}^{1/3}(t)$	36.76
$\mathcal{M}_2^f:$	$\omega_0^2 = \omega_{n_f}^2 + \delta_f \mathcal{Q}^{1/3}(t) + \gamma_f \mathcal{Q}^{5/3}(t)$	43.64
$\mathcal{M}_3^f:$	$\omega_0^2 = \omega_{n_f}^2 + \delta_f \mathcal{Q}^{1/3}(t) + \alpha_f \mathcal{Q}^2(t)$	43.72

Then, global sensitivity analysis is performed to assess which parameters have most influence on the model $\mathcal{M}_1^f$ response. It is assumed that each parameter follows a Uniform distribution $\mathcal{U}(a, b)$, with $a = (1 - \Delta)$ its minimum and $b = (1 + \Delta)$ its maximum value, whereas $\Delta = 10\%$. The supports are determined based on the deterministic values $\hat{\boldsymbol{\Theta}}$ obtained after the model selection step. The supports are indicated in Table 5.

Table 5: Uniform prior distribution $\mathcal{U}(a, b)$ of the model $\mathcal{M}_1^f$ parameters for global sensitivity analysis.

Support	ω_{n_f} [rad/s]	$\delta_f \times 10^5$ [N/(m^{3}kg)]
a	344.67	-2.9103
b	381.05	-2.3811

The total and partial variances of each parameter were calculated based on Monte-Carlo simulations, since only two parameters are being evaluated. Fig. 9 depicts the total and first-order Sobol' indices. These results lead to conclusions: parameter ω_{n_f} has considerable influence on the model $\mathcal{M}_1^f$, whereas varying the parameter δ_f within its adopted support has little influence on the model's predictive ability. For this reason, the parameter δ_f is considered as a determined quantity and its value is set to $\delta_f = -2.6457 \times 10^5$. In contrast, the variability of the parameter ω_{n_f} requires attention, and its posterior distribution is calibrated using the Bayesian inference framework.
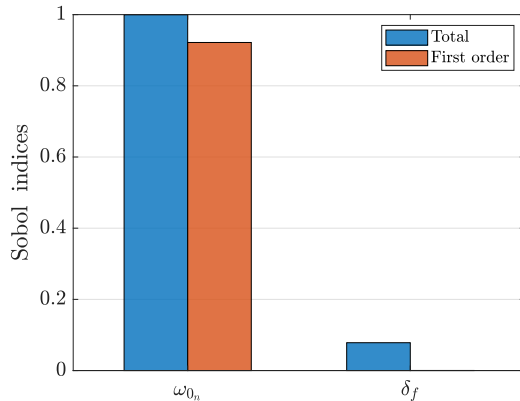

Fig. 9: Prior global sensitivity analysis. Total and first order Sobol' indices of parameters ω_{n_0} and δ_f.

In addition to ω_{n_f}, the variance σ_ε^2 is also considered as a random parameter and its values are adjusted with the MCMC/Metropolis-Hastings algorithm. For both parameters, the prior distribution is assumed Uniform, such that the supports for ω_{n_f} remain as those indicated by Table 5, and $\sigma_\varepsilon^2 \sim \mathcal{U}\big(5 \times 10^{-4}, 2 \times 10^{-3}\big)$. A Markov chain containing $n_s = 1200$ samples was generated (burn-in of 10 %). Then, the random walk step σ_p was fixed to 0.07 (acceptance rate of $\approx 45\%$). These results also ensured the convergence of the chain.

Importantly, for Bayesian calibration, 16 free response data for different initial conditions were considered, whereas the remaining 4 are used for validation of the stochastic model.

Figs. 10(a)-(b) show the prior and posterior PDFs of ω_{n_0}[1] and σ_ε^2, respectively. Statistical aspects of both distributions are present in Table 6, which includes the MAP and mean μ values for each PDF from Fig. 10, in addition to the deterministic result $\hat{\boldsymbol{\Theta}}$ for ω_{n_0} obtained in the previous step. Note that both the MAP and the mean mean μ are close to the deterministic estimate obtained by least-squares method, indicating that the approach adopted by this work to propose prior distributions is adequate.

To quantify how much information is lost if knowledge was based only on the prior distribution, the Kullback-Leibler (KL) divergence is calculated and the results are also included in this table. The divergence values are around $D_{kl}(\text{posterior}||\text{prior}) \approx 0.875$ for ω_{n_0}, and ≈ 0.156 for σ_ε^2, indicating that posterior PDFs have added a considerable amount of information, especially for the first parameter, in comparison with the Uniform ones. For measuring the dispersion of distributions, another useful statistical measure is the coefficient of variation (CoV) related to each parameter: the CoV for the frequency parameter is less than 1%, whereas for σ_ε^2 the value is around 10%, indicating that there is greater uncertainty about the estimation of this parameter. With respect to the shape of these PDFs, for ω_{n_0}, an unimodal PDF was identified, being concentrated around this unique mode; PDF of σ_ε^2, in turn, resulted in a bimodal distribution.

---

[1]To bring physical insight into the values of this parameter, the distributions are shown considering the unit as [Hz] instead of [rad/s].

Fig. 11 presents the frequency backbone curves obtained by the calibrated model with confidence intervals with respect to experimental measurements for four different initial conditions. These curves indicate that the regression model obtained is valid and able to reproduce the experimental backbones within its confidence intervals. The nonlinear softening effect is also well captured by the numerical model due to the negative δ_f coefficient. Note that the data used for validation were not considered during the Bayesian updating.
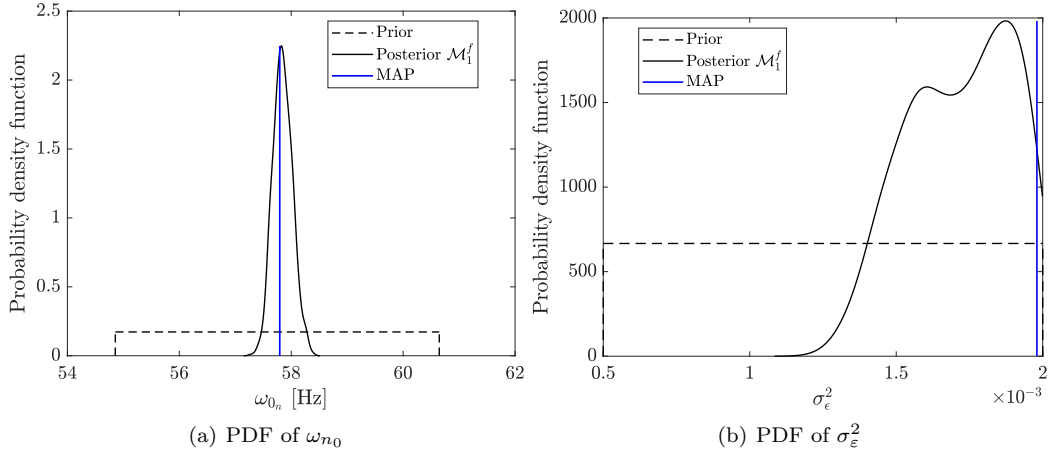

(a) PDF of ω_{n_0} (b) PDF of σ_ε^2

Fig. 10: PDFs of the random variables ω_{n_0} and σ_ε^2. −− is the prior, — the posterior and — represents the MAP value.

Table 6: MAP estimator, mean value μ, initial estimate $\hat{\mathbf{\Theta}}$, Kullback-Leibler divergence and CoV for each random variable of the frequency model.

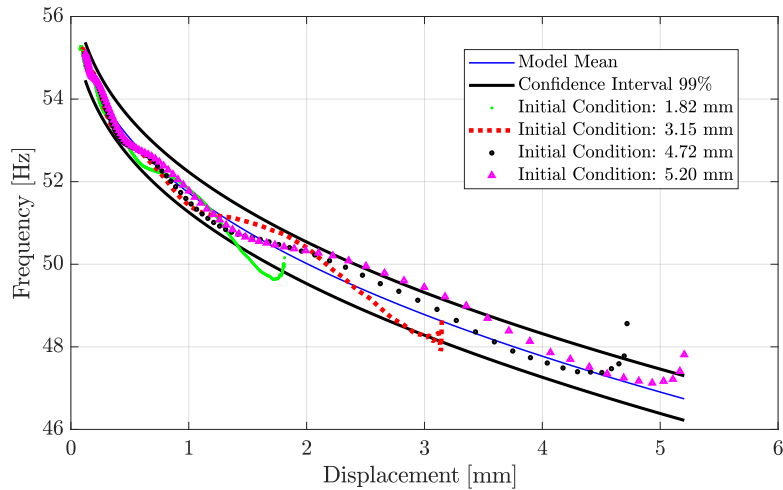| Parameter	MAP	μ	$\hat{\mathbf{\Theta}}$	$D_{kl}(\text{posterior}||\text{prior})$	CoV [%]
ω_{0_n}	363.29 (57.82 Hz)	363.45 (57.84 Hz)	363.31(57.82 Hz)	0.875	0.28
σ_ε^2	1.99×10^{-3}	1.77×10^{-3}	-	0.156	10.5

Fig. 11: Frequency backbone curves considering different initial conditions.

5.2. Damping backbone calibration

Having the frequency model established, the next step is to select the most appropriate model to reproduce the experimental damping curves. Once again, the polynomial basis described by Eq. (11) is used to generate candidate models. Table 7 presents the models[2] obtained after regression on damping data. Note that selecting

---

[2]To simplify the notation, the frequency dependence is not included in this table.

among these models based only on AIC values is not recommended, since considering only deterministic estimates of their parameters, the three models deliver nearly the same performance. Thus, to prevent the identification process from suffering bias, all models are calibrated by the Bayesian framework.

Table 7: Models obtained after regression on damping data (experimental measurements) and their respective AIC values.

Model		AIC
$\mathcal{M}_1^d$:	$\xi = \xi_{0_d} + \lambda_d \mathcal{Q}(t) + \kappa_d \mathcal{Q}^{4/3}(t) + \gamma_d \mathcal{Q}^{5/3}(t) + \alpha_d \mathcal{Q}^2(t)$	192.59
$\mathcal{M}_2^d$:	$\xi = \xi_{0_d} + \beta_d \mathcal{Q}^{2/3}(t) + \kappa_d \mathcal{Q}^{4/3}(t) + \gamma_d \mathcal{Q}^{5/3}(t) + \alpha_d \mathcal{Q}^2(t)$	193.00
$\mathcal{M}_3^d$:	$\xi = \xi_{0_d} + \beta_d \mathcal{Q}^{2/3}(t) + \lambda_d \mathcal{Q}(t) + \kappa_d \mathcal{Q}^{4/3}(t)$	193.12

Before proceeding to the MCMC/Metropolis-Hastings algorithm, sensitivity analysis is carried out to evaluate the most influential parameters that consequently require calibration. For each model, a Uniform distribution $\mathcal{U}(a, b)$ is assigned to each of its parameters based on the estimation obtained by the least-squares method, such that $\Delta = 10\%$ was employed. Fig. 12 shows the Sobol indices of the models' parameters. Although some of the parameters are present in more than one model, their influence is not the same, as is the case for the parameter κ_d. For models $\mathcal{M}_1^d$ and $\mathcal{M}_2^d$, this parameter has high total Sobol indices, around 0.82 and 0.76 respectively, and is therefore considered as a parameter that requires attention and, for both cases, needs to be calibrated by the Bayesian inference. On the other hand, note that this same parameter is also present in model $\mathcal{M}_3^d$ with a total index of 0.21, i.e., it can be considered as a determinate variable for this model. The responsible for such variations is the structure of the models, such that the weight of the parameter is impacted by the other terms present in the polynomial approximation. In this work, all parameters with Sobol index greater than 0.25 have their posterior probability distributions estimated by the Bayesian inference, whereas the others are taken as determinate variables with values set to the estimate found by the least-squares method. Note that the term 'determinate variables' is employed to denote those parameters with low influence on the system's output, as determined through sensitivity analysis, and does not necessarily imply deterministic variables.
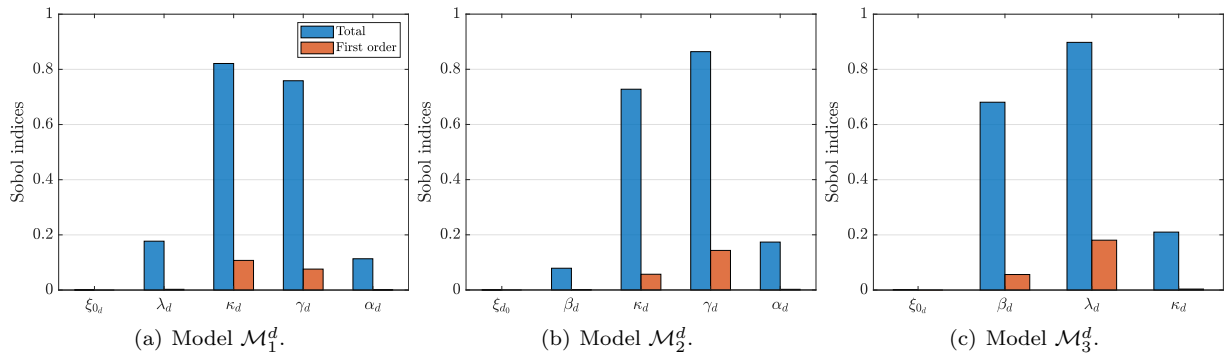

(a) Model $\mathcal{M}_1^d$.   (b) Model $\mathcal{M}_2^d$.   (c) Model $\mathcal{M}_3^d$.

Fig. 12: Prior global sensitivity analysis performed on three model candidates for damping.

Fig. 13 shows the probability distribution function marginal likelihood derived from the mean absolute scaled error between each candidate model and experimental data. The Bayesian approach to model selection reveals its benefits: note that the marginal likelihood for the simplest model with relatively fewer parameters has higher values than for the most complex models. In general, the more complex models are able to replicate a larger amount of data. However, since the marginal likelihood must be normalized, they are penalized in the region where all models are able to replicate the same data, showing smaller values of the marginal likelihood with a wider shape. Green and Worden [40] provided an insightful discussion on this subject. For each model,

a Markov chain containing $n_s = 2000$ samples was generated (burn-in of 10 %) and the acceptance rate was adjusted around 40%, ensuring convergence of the chains.
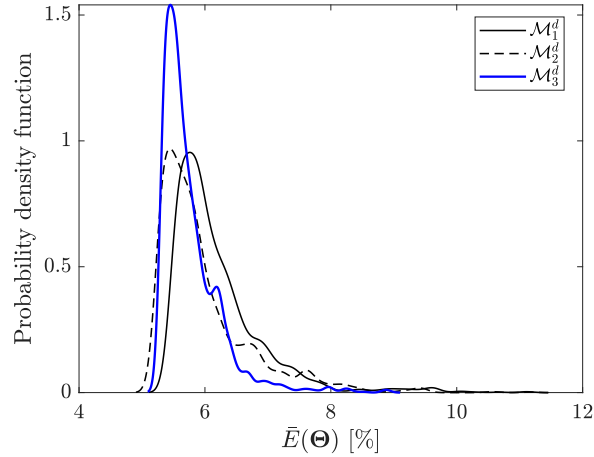

Fig. 13: Marginal likelihood derived from the mean absolute scaled error between models and experimental data.

From the PDFs presented in Fig. 13, the Bayesian Information Criterion (BIC) was estimated to provide quantitative evidence about the model structures and its values are shown in Table 8. It is important to point out that the quantity calculated by BIC is different from that obtained by AIC, and their scores for the case investigated in this work are inversely proportional, which means that AIC prioritized models with a greater fit to the data. The BIC penalizes the model more for its complexity, i.e., more complex models have higher scores. Therefore, from the marginal likelihood and the values obtained by the BIC score, the model selected to describe the damping data is model $\mathcal{M}_3^d$. Note that among the candidate models, the selected one presents less complexity in terms of the number of coefficients. Moreover, considering only the training data, the mean absolute scaled error for $\mathcal{M}_3^d$ is 5.44%.

Table 8: BIC scores for each model candidate.

Model	BIC
$\mathcal{M}_1^d$	161.95
$\mathcal{M}_2^d$	157.52
$\mathcal{M}_3^d$	145.68

Figs. 14(a), (b) and (c) depict the prior and posterior PDFs of β_d, λ_d and σ_ε^2, respectively. Table 9 concentrates the main statistical metrics extracted from these distributions. Once again, the MAP and mean values obtained after Bayesian inference are close to those estimated by the least-squares method. It is noteworthy that, among all the parameters, the one that obtained he one that obtained more information regarding its prior distribution is the parameter σ_ε^2, although it is also the estimate with the highest uncertainty. Proposing supports for this parameter can be challenging, and involves expertise. If high values for the support are adopted, the model obtained may become more uncertain (this parameter is associated with the error dispersion in the model, see Eq. (5) and with wider confidence intervals.

Since the estimation for the damping backbone involves the presence of more than one model coefficient in the calibration process of the posteriors, it is desirable to evaluate the existence or not of correlation between parameters. Fig. 15 shows the Pearson's correlation coefficient for λ_d and β_d. Bearing in mind that this coefficient can assume values from -1 (inversely correlated) to 1 (correlated), where 0 indicates there is no correlation, it can be seen that none of the model coefficients are correlated with σ_ε^2, and that between them,
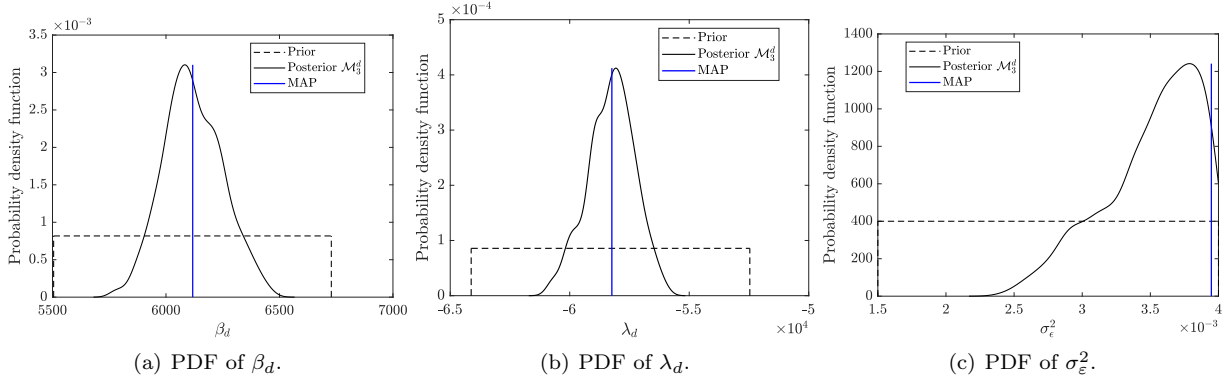
(a) PDF of β_d.   (b) PDF of λ_d.   (c) PDF of σ_ε^2.

Fig. 14: PDFs of the random variables β_d, λ_d and σ_ε^2. $--$ is the prior, ▬ the posterior and ▬ represents the MAP value.

Table 9: MAP estimator, mean value μ, initial estimate $\hat{\Theta}$, Kullback-Leibler divergence and CoV for each random variable of the damping model.

Parameter	MAP	μ	$\hat{\Theta}$	$D_{kl}(\text{posterior}||\text{prior})$	CoV [%]
β_d	6117.8	6119.1	6116.8	0.16	2.11
λ_d	-58237	-58262	-58294	0.13	1.68
σ_ε^2	3.94×10^{-3}	3.51×10^{-3}	-	0.30	10.29

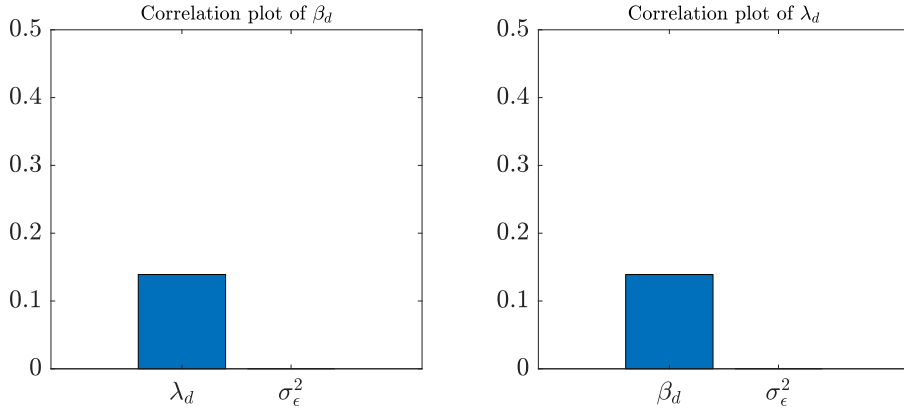the correlation is low.

Fig. 15: Correlation plot for β_d and λ_d parameters based on the Pearson coefficient. Results indicate low correlation between parameters

Fig. 16 shows the damping backbone curves obtained by the model and their respective 99% confidence intervals for different initial conditions. The results indicate that the model predictions accommodate the experimental measurements. However, the model is not able to reproduce the drop seen in the damping values - the model mean does not fully represent the observed physical behavior.
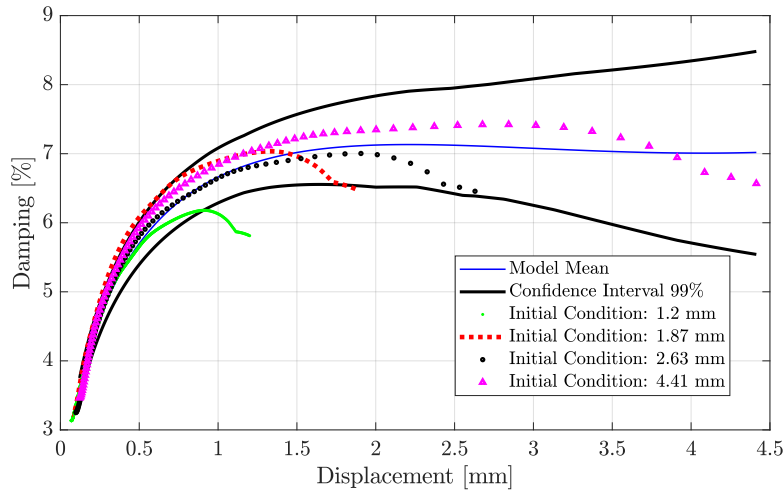
18

Fig. 16: Damping backbone curves considering different initial conditions.

6. Identification of the Payne Effect using Bayesian Identification

The Payne effect identification process combines the Bayesian identification results presented in section 5, and a numerical twin of the experimental set-up. The complete process is detailed in Fig. 18, and it is based on both the experimental set-up ① as well as the digital model of this set-up ②. The main steps indicated in the text as ⦿ can be positioned on this figure.

6.1. Experimental Set-up ①

The experimental frequency backbones identified in section 5, and presented in Fig. 6, are used to quantify the frequencies f_{exp} ③ in the free vibratory response of the polymer. The frequency band is placed 46 Hz and 56 Hz.

6.2. Digital Twin ②

The digital twin is a 2D Finite Element-based model of the experimental set-up built in COMSOL Multiphysics ®(Fig.17). This 2D model assumes plane stress and incorporates two metallic skin plates, the polymer sample; the clamper base and the accelerometer are also modelled for a better representation of the test configuration. The metallic skins are made of stainless steel, with properties of $E = 210$ GPa for the elastic Young modulus, $\nu = 0.29$ for the Poisson ratio and 7800 kg/m^3 for the density. The viscoelastic polymer sample is represented with an unknown storage modulus ranging from 4 MPa to 30 MPa and a loss factor of 0.49. The variations of the loss factor estimated from the experimental identification have been taken into account (Fig. 7), but the results show that these variations lead to a frequency variation of less than 0.06 %. The rest of the work was therefore conducted on the basis of modulus variations only. A prescribed displacement is imposed on the clamper.

A parametric modal analysis carried out on the digital twin, varying the storage modulus of the polymer material, allows to estimate the evolution of the first natural frequency as a function of the modulus. By inverting the curve, the digital model thus enables the determination of how the modulus evolves with respect to frequency ④.
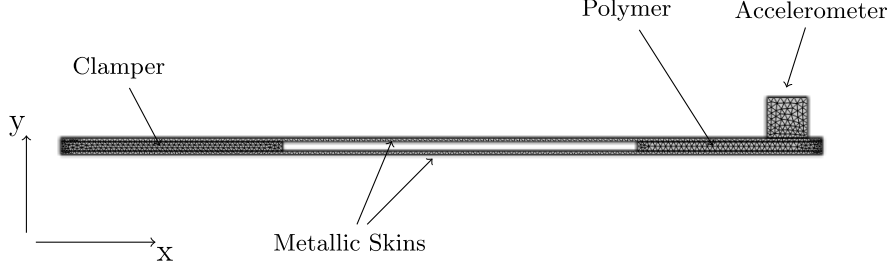
19

Fig. 17: The digital twin model is a 2D Finite Element model under the plane stress assumption.

6.3. Combination of experiments and numerical results for identification of the Payne effect

After identifying the frequency range of interest ③, and having the evolution of the storage modulus with frequency known ④, both are combined to estimate the evolution of the storage modulus on the frequency range of interest $E(f_{exp})$. For each value of the storage modulus E, an initial displacement Disp^{num} is applied in the y-direction, allowing for the computation of constant shear strains $\text{Strain}^{\text{num}}$ within the sample, facilitated by the digital twin model. The homogeneity of the shear strains in the sample is numerically validated, ensuring its accuracy. These quantities are used to create a ratio R, defined as

$$R(E) = \frac{\text{Strain}^{\text{num}}(\text{E})}{\text{Disp}^{\text{num}}(\text{E})}. \tag{14}$$
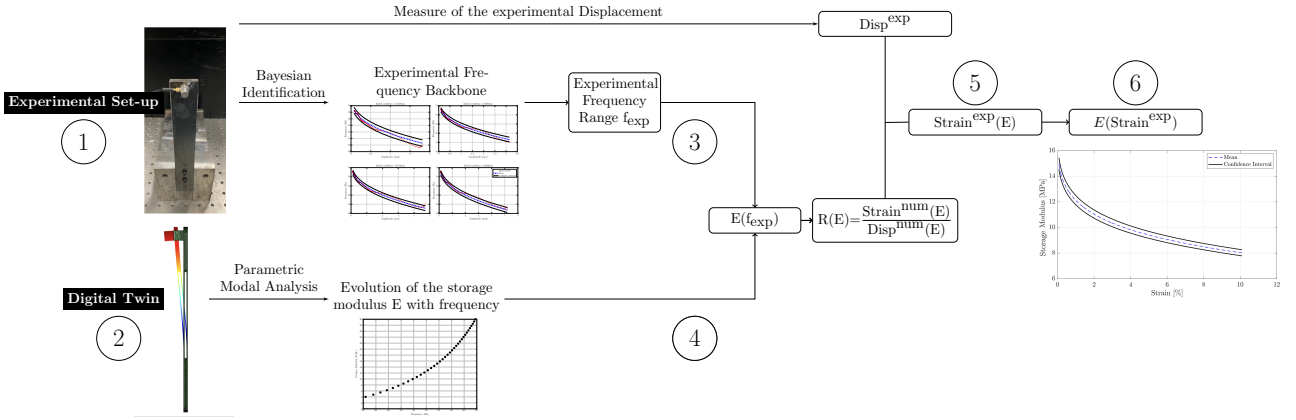

Fig. 18: Process for the identification of the Payne effect.

By leveraging this ratio alongside the experimentally measured displacement, it becomes feasible to estimate deformations $\text{Strain}^{\text{exp}}$ occurring within the characterized sample ⑤.

As the estimation of the experimental strain is done for different values of the storage modulus, the link between these quantities is established.The obtained dependency of the storage modulus on the shear strain rate, known as the Payne effect, is illustrated in Fig. 20. The Bayesian identification conducted to estimate the experimental frequencies enables the quantification of both the mean value and the standard deviation, or a 99% confidence interval, for the Payne effect. The results obtained demonstrate a high confidence level with a narrow confidence interval centered around the mean value.
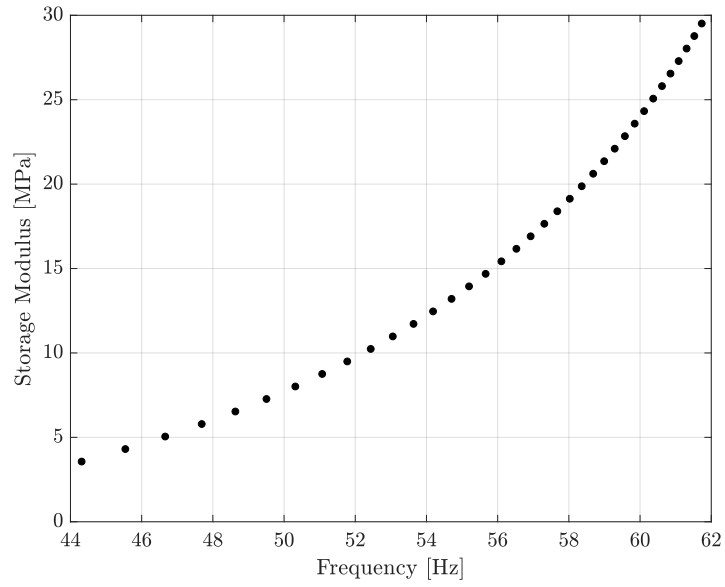
Fig. 19: Evolution of the Storage Modulus of the sample with the first eigenfrequency, from the digital twin of the experimental setup.
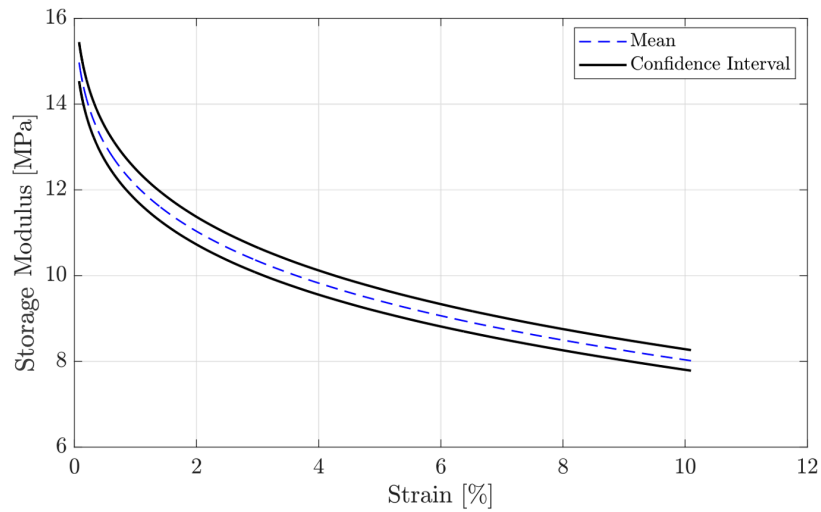

Fig. 20: Identification of the Payne effect

7. Final Remarks

This research work aims to propose an approach to quantify the Payne effect in a polymer material. First, a modified Oberst experiment has been implemented to characterize the dynamic behavior of an elastomeric material under different stress amplitudes. The dynamic properties of the structure, frequency and damping of the first mode, are identified by applying a Bayesian inference approach which allows to quantify the selection of the models allowing to maximize the a posteriori probability, and to quantify their confidence level.

A digital twin of the experimental set-up is then developed and coupled to the experimental results, to estimate the strain level in the characterized sample, and identify the Payne effect. As expected, this results in a decrease of the storage modulus with the stress amplitude, and the results show that the confidence level is good with a small confidence interval around the mean value.

The strength of the proposed approach lies in the combination of experimental data that can be collected rapidly, of a digital twin of the experimental set-up, and of a Bayesian identification process for quantifiying the complex nonlinear behavior of a viscoelastic material with its uncertainty.

CRediT authorship contribution statement

Kévin Jaboviste: Investigation, Experimental tests, Formal analysis, Writing - review and editing; **Emeline Sadoulet-Reboul:** Formal analysis, Writing - original draft, review and editing; **Rafael Teloli:** Software curation, Formal analysis, Writing - original draft, review and editing; **Gaël Chevallier:** Conceptualization, Writing - review and editing.

Declaration of Competing Interest

The authors declare that they have no known competing financial interests or personal relationships that could have appeared to influence the work reported in this paper.

Acknowledgments

Appendix A. Sliding Least-Squares identification Method

This appendix details the post-processing of the experimental data and the sliding least-squares identification method applied to recover the evolution of the instantaneous damping and frequency, as used in [30], [41]. Having the raw acceleration data in Fig. A.1(a), Figs. A.1(b) to (e) depict the steps used to exploit the measured signal and obtain the instantaneous frequency and the damping according to the oscillation time (Figs. A.1(f)). A brief description of each step is outlined below:

- **Fig. A.1(b):** The raw acceleration signal is integrated twice by using the trapezium rule to result in the displacement. The time increment Δt used is equal to $1/F_s$, whereas F_s denotes the sampling frequency which, in this work, it was set to $Fs = 51200$ Hz. Notwithstanding, experimental data is often corrupted by noise which, when numerically integrated, results in a spurious mean level that has to be disregarded.

This operation is performed by removing the DC component from the displacement after the integration scheme. The underlying assumption that holds in structural dynamics is that the system oscillates around its equilibrium position.

- **Fig. A.1(c):** The displacement signal obtained has response contributions not only from the first bending mode. Thus, to filter out this frequency component from the others that compose the signal, the Empirical Mode Decomposition (EMD) method [42] is used. This approach relies on identifying the characteristic time scales that are embedded in the oscillatory response through the Intrinsic Mode Functions (IMF), or also known as intrinsic modes. The construction of the IMFs is based on a cubic spline interpolation of the upper and lower envelopes of the time series signal. By subtracting the average between envelopes $m_1(t)$ from the initial response signal $x(t)$, the first IMF is obtained $h_1(t) = x(t) - m_1(t)$; this component must satisfy two properties:

  - The number of extremes and passages through the equilibrium must be equal or differ from 1 at most.
  - At all points, the average value of the envelopes defined by the local maximums and minimums must be 0.

  The IMF construction is iteratively solved: if the mode does not hold these properties, the algorithm is repeated on the updated $h_1(t)$ until finding a component that satisfies them. This is a critical step in ensuring that each IMF is a monochromatic signal for which amplitude and frequency can still be modulated. The number of IMFs to be extracted is established with a stopping criterion, which can be formulated in terms of energy. It is important to point out that when considering the free response of a system, these IMFs have physical meaning: the dominant IMFs correspond to the vibrating modes of the structure, and they can be analytically rewritten as equivalent single-degree-of-freedom linear oscillators. For nonlinear systems, this assumption holds for weakly nonlinearities with no modal interactions.

- **Fig. A.1(d):** Once the IMF corresponding the first bending mode of the Oberst beam is well extracted, the evolution of instantaneous frequency and damping as a function of time can then be computed. Assuming that the EMD does indeed allow a modal decoupling, the weakly nonlinear response can be written as:

$$\ddot{q} + 2\xi(\mathcal{Q})\omega_0(\mathcal{Q})\dot{q} + \omega_0^2(\mathcal{Q})q = 0, \tag{A.1}$$

where, in this second order differential equation, ξ and ω_0 depend directly on the amplitude $\mathcal{Q}$ of the time response $q(t)$. To simplify the notations, the dependence of these parameters on $\mathcal{Q}$ will be implicit. The solution of Eq. (A.1) yields:

$$q(t, \xi, \omega_0) = \mathcal{Q}(t) \cos(\omega_r t + \phi), \tag{A.2}$$

where the envelope is $\mathcal{Q}(t)$ is given by:

$$\mathcal{Q}(t) = \mathcal{Q}_0 e^{-\xi\omega_0 t}. \tag{A.3}$$

Rewriting Eq. (A.2) by sinus and co-sinus terms:

$$q(t, \xi, \omega_0) = e^{-\xi\omega_0 t} \left(A \cos(\omega_r t) + B \sin(\omega_r t) \right), \tag{A.4}$$

23

where $\omega_r = \omega_0\sqrt{1-\xi^2}$ is the damped frequency, and A and B are amplitude coefficients:

$$A = \mathcal{Q}_0, \quad \text{and} \quad B = \frac{\dot{\mathcal{Q}}_0 + \xi\omega_0\mathcal{Q}_0}{\omega_d},$$

where $\mathcal{Q}_0$ and $\dot{\mathcal{Q}}_0$ denote the initial displacement and velocity, respectively. The measured signal is approximated by the analytical solution over a window representing a period. The identification of the parameters ξ and ω_0 over this period is done by minimizing, in the sense of least-squares approach, the following objective function:

$$F_{obj} = \min_{\omega_0,\xi} \sum_{i=1}^{n} \left(q(t_i, \xi, \omega_0) - q_{exp}(t_i) \right)^2 \tag{A.5}$$

where q represents the analytical form (A.1) of the displacement, q_{exp} the experimental displacement that corresponds to the first IMF extracted from oscillatory response; t_i, for $i \in [1, n]$, denotes the time steps included in the period $[t; t + dt]$ that compose the sliding window. The coefficients A and B are updated taking into account the initial conditions of displacement and velocity for each window.

- **Fig. A.1(e) and (f)** This identification approach based on the sliding least-squares method renders possible to track the instantaneous variations of the damping ξ and the frequency ω_0 to reconstruct the experimental signal as well as its envelope. Put practically, this is more of an "average" instantaneous frequency than an instantaneous frequency in the sense of that provided by the Hilbert transform. These figures also illustrate how the Oberst beam behaves, such that the amplitude decreases with time while the instantaneous frequency increases, going from 46 Hz to 55 Hz, and that the damping seems to go through a maximum around 8% before decreasing to tend around 3%. Note that when the displacement is around zero, the damping measurement becomes influenced by noise.
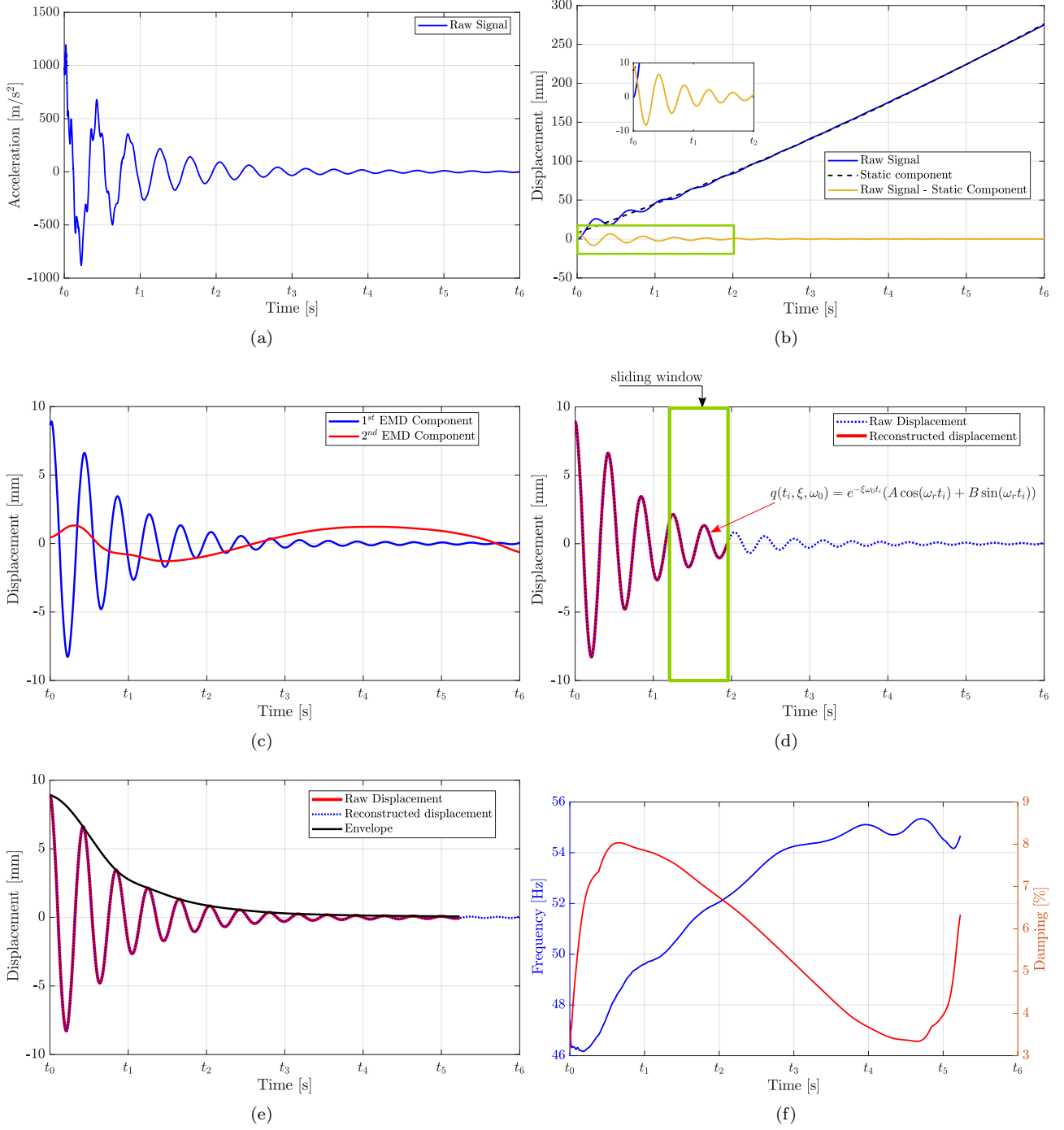
24

Figure A.1: Post-treatment process : raw acceleration (a), raw displacement and continuous component (b), EMD on the displacement without the continuous component (c), identification of the instantaneous frequency and the modal damping by a sliding least square method (d), reconstruction of the experimental displacement (e) and instantaneous frequency and damping ratio evolution according to the time (f)

Appendix B. Bayesian Linear Regression Formulation

The authors thank the reviewer who pointed out the existence of analytical solutions for the Bayesian linear regression case investigated in this article. For this case, in which the models for frequency and damping are linear in their parameters (although not linear with respect to the displacement), it is possible to derive analytical expressions for the posterior distributions of the model parameters $\mathbf{\Theta}$ and also the variance σ^2, a parameter that is also assumed as unknown in this work. Under the hypothesis of additive decorrelated Gaussian noise,

the following presents the joint posterior distributions for the regression problem presented in equation (2)[3]:

$$\pi\left(\boldsymbol{\Theta}, \sigma_\varepsilon^2 | \mathcal{D}\right) \propto \pi(\boldsymbol{\Theta}, \sigma_\varepsilon^2)\pi(\mathcal{D}|\boldsymbol{\Theta}, \sigma_\varepsilon^2), \tag{B.1}$$

where $\pi(\boldsymbol{\Theta}, \sigma_\varepsilon^2)$ corresponds to the prior distribution. Considering an uninformative prior distribution such that $\pi(\boldsymbol{\Theta}, \sigma_\varepsilon^2) \propto \frac{1}{\sigma^2}$ which is a flat prior almost uniform, the resulting marginal posterior distributions for $\boldsymbol{\Theta}$ and σ^2 are given by:

$$\pi(\boldsymbol{\Theta}|\mathcal{D}) \sim t_{N-p}\left(\hat{\boldsymbol{\Theta}}, \frac{\left(\mathcal{D} - \mathcal{D}^{\mathcal{M}}(\boldsymbol{\Theta})\right)^T\left(\mathcal{D} - \mathcal{D}^{\mathcal{M}}(\boldsymbol{\Theta})\right)}{N-p}\left(\mathcal{X}^T\mathcal{X}\right)^{-1}\right), \tag{B.2}$$

$$\pi(\sigma_\varepsilon^2|\mathcal{D}) \sim \text{Inv-Gamma}\left(\frac{N-p}{2}, \left[\frac{1}{2}\left(\mathcal{D} - \mathcal{D}^{\mathcal{M}}(\boldsymbol{\Theta})\right)^T\left(\mathcal{D} - \mathcal{D}^{\mathcal{M}}(\boldsymbol{\Theta})\right)\right]^{-1}\right), \tag{B.3}$$

i.e., the marginal posterior distribution $\pi(\boldsymbol{\Theta}|\mathcal{D})$ results in a multivariate $t-student$ distribution, and $\pi(\boldsymbol{\sigma}_\varepsilon^2|\mathcal{D})$, an inverse gamma distribution. In both equations, p corresponds to the number of model parameters, and the expected value of $\boldsymbol{\Theta}$ is given by:

$$\hat{\boldsymbol{\Theta}} = \int_{\boldsymbol{\Theta}, \sigma_\varepsilon^2} \boldsymbol{\Theta}\pi(\boldsymbol{\Theta}, \sigma_\varepsilon^2|\mathcal{D})d\boldsymbol{\Theta}d\sigma_\varepsilon^2, \tag{B.4}$$

which corresponds to the least-squares estimate.

Tables B.1 and B.2 present the results obtained by the MAP estimator considering the results derived analytically by expressions (B.2)-(B.3) and the ones obtained by the MCMC/Metropolis Hastings algorithm. Note that, for this method, a uniform distribution for the model parameters Θ and the variance σ_ε^2 is adopted. In the scenario investigated in this work, where a large amount of data is available, the use of a uniform distribution to derive the closed-form solutions yields a t-student PDF for the model parameters and also an inverse gamma for σ_ε^2. As the amount of data available increases, the influence of the prior decreases in relation to the likelihood. Consequently, the analytical results directly align with those obtained via the MCMC/Metropolis-Hastings algorithm. Moreover, both methodologies yield close values for the frequency and damping models.

Table B.1: MAP estimator for each random variable of the frequency model considering the analytical PDF and the one obtained by the MCMC/Metropolis-Hastings algorithm.

ω_{0_n} [Hz]	$\delta_f \times 10^5$ [N/(m^{3}kg)]	Method
57.8	-2.643	Analytic
57.8	-2.645	MCMC/Metropolis Hastings

Table B.2: MAP estimator for each random variable of the damping model considering the analytical PDF and the one obtained by the MCMC/Metropolis-Hastings algorithm.

ζ_{0_d}	β_d	λ_d	$\kappa_d \times 10^5$	Method
3.56	6221	-59353	1.510	Analytic
3.56	6117	-58237	1.512	MCMC/Metropolis Hastings

---

[3]These results can be used for the same class of problem without loss of generality

References

[1] X. Zhou, D. Yu, X. Shao, S. Zhang, S. Wang, Research and applications of viscoelastic vibration damping materials: A review, Composite Structures 136 (2016) 460–480. `doi:https://doi.org/10.1016/j.compstruct.2015.10.014`.

[2] K. Liu, S. Tang, L. Zhu, W. Wen, M. Liu, H. Li, C. Zhou, B. Luo, Bio-inspired liquid crystal gel with adjustable viscoelasticity to modulate cell behaviors and fate, Composites Part B: Engineering 234 (2022) 109704. `doi:https://doi.org/10.1016/j.compositesb.2022.109704`.

[3] L. Mullins, Softening of Rubber by Deformation, Rubber Chemistry and Technology 42 (1) (1969) 339–362. `doi:https://doi.org/10.5254/1.3539210`.

[4] A. R. Payne, R. E. Whittaker, Low strain dynamic properties of filled rubbers, Rubber Chemistry and Technology 44 (2) (1971) 440–478.

[5] W. P. Fletcher, A. N. Gent, Nonlinearity in the dynamic properties of vulcanized rubber compounds, Rubber Chemistry and Technology 27 (1) (1954) 209–222.

[6] R. Österlöf, H. Wentzel, L. Kari, N. Diercks, D. Wollscheid, Constitutive modelling of the amplitude and frequency dependency of filled elastomers utilizing a modified boundary surface model, International Journal of Solids and Structures 51 (19) (2014) 3431–3438. `doi:https://doi.org/10.1016/j.ijsolstr.2014.06.003`.

[7] K. Jaboviste, E. S. Reboul, N. Peyret, G. Chevallier, C. Arnould, E. Collard, Identification of nonlinear viscoelastic parameters based on an enhanced oberst beam method, in: G. Kerschen (Ed.), Nonlinear Dynamics, Volume 1, Springer International Publishing, Cham, 2019, pp. 379–382.

[8] Z. Xu, Y. Song, Q. Zheng, Payne effect of carbon black filled natural rubber compounds and their carbon black gels, Polymer 185 (2019) 121953. `doi:https://doi.org/10.1016/j.polymer.2019.121953`.

[9] X. Shi, S. Sun, A. Zhao, H. Zhang, M. Zuo, Y. Song, Q. Zheng, Influence of carbon black on the payne effect of filled natural rubber compounds, Composites Science and Technology 203 (2021) 108586. `doi:https://doi.org/10.1016/j.compscitech.2020.108586`.

[10] J. Frohlich, W. Niedermeier, H. D. Luginsland, The effect of filler–filler and filler–elastomer interaction on rubber reinforcement, Composites Part A: Applied Science and Manufacturing 36 (4) (2005) 449–460.

[11] H. Gacem, Y. Chevalier, J. Dion, M. Soula, B. Rezgui, Nonlinear dynamic behaviour of a preloaded thin sandwich plate incorporating visco-hyperelastic layers, Journal of sound and vibration 322 (4-5) (2009) 941–953.

[12] M. Rendek, A. Lion, Strain induced transient effects of filler reinforced elastomers with respect to the Payne-effect: experiments and constitutive modelling, ZAMM - Journal of Applied Mathematics and Mechanics / Zeitschrift für Angewandte Mathematik und Mechanik 90 (5) (2010) 436–458. `doi:https://doi.org/10.1002/zamm.200900362`.

[13] W. Luo, X. Hu, C. Wang, Q. Li, Frequency- and strain-amplitude-dependent dynamical mechanical properties and hysteresis loss of CB-filled vulcanized natural rubber, International Journal of Mechanical Sciences 52 (2) (2010) 168–174, sPECIAL ISSUE: Advances in Modeling and Evaluation of Materials in Honor of Professor Tomita. doi:https://doi.org/10.1016/j.ijmecsci.2009.09.001.

[14] H. Jrad, J. L. Dion, F. Renaud, I. Tawfiq, M. Haddar, Experimental characterization, modeling and parametric identification of the non linear dynamic behavior of viscoelastic components, European Journal of Mechanics-A/Solids 42 (2013) 176–187.

[15] F. Renaud, G. Chevallier, J.-L. Dion, R. m. Lemaire, Viscoelasticity measurement and identification of viscoelastic parametric models, in: International Design Engineering Technical Conferences and Computers and Information in Engineering Conference, Vol. 54785, 2011, pp. 701–708.

[16] I. H. Syed, P. Vouagner, F. Fleck, J. Lacayo-Pineda, Nonlinearity in the mechanical response of rubber as investigated by high-frequency DMA, Polymers 11 (4). doi:https://doi.org/10.3390/polym11040581.

[17] R. Esmaeeli, T. Tada, S. Farhad, A new high frequency dynamic mechanical analysis system: An approach to direct high frequency testing of tire tread rubber, Polymer Testing 86 (2020) 106491.

[18] J.-L. Wojtowicki, L. Jaouen, R. Panneton, New approach for the measurement of damping properties of materials using the oberst beam, Review of Scientific Instruments 75 (8) (2004) 2569–2574. doi:10.1063/1.1777382.

[19] A. E756-98, Standard test method for measuring vibration-damping properties of materials, American Society for Testing and Materials.

[20] M. S. Ozer, H. Koruk, K. Y. Sanliturk, Testing non-magnetic materials using Oberst Beam Method utilising electromagnetic excitation, Journal of Sound and Vibration 456 (2019) 104–118. doi:https://doi.org/10.1016/j.jsv.2019.05.029.

[21] Y. Liao, V. Wells, Estimation of complex Young's modulus of non-stiff materials using a modified Oberst beam technique, Journal of Sound and Vibration 316 (1) (2008) 87–100. doi:https://doi.org/10.1016/j.jsv.2008.02.028.

[22] P. Prasob, M. Sasikumar, Static and dynamic behavior of jute/epoxy composites with zno and tio2 fillers at different temperature conditions, Polymer Testing 69 (2018) 52–62. doi:https://doi.org/10.1016/j.polymertesting.2018.04.040.

[23] T. L. Attard, L. He, H. Zhou, Improving damping property of carbon-fiber reinforced epoxy composite through novel hybrid epoxy-polyurea interfacial reaction, Composites Part B: Engineering 164 (2019) 720–731. doi:https://doi.org/10.1016/j.compositesb.2019.01.064.

[24] A. Joy, S. Varughese, A. K. Kanjarla, S. S., P. Haridoss, Effect of the structure and morphology of carbon nanotubes on the vibration damping characteristics of polymer-based composites, Nanoscale Adv. 2 (2020) 1228–1235. doi:http://dx.doi.org/10.1039/C9NA00812H.

[25] B. Tang, M. Brennan, G. Gatti, N. Ferguson, Experimental characterization of a nonlinear vibration absorber using free vibration, Journal of Sound and Vibration 367 (2016) 159–169. doi:https://doi.

org/10.1016/j.jsv.2015.12.040.

URL https://www.sciencedirect.com/science/article/pii/S0022460X15010524

[26] B. Tang, S. Wang, M. J. Brennan, L. Feng, W. Chen, Identifying the stiffness and damping of a nonlinear system using its free response perturbed with gaussian white noise, Journal of Vibration and Control 26 (9-10) (2020) 830–839. doi:https://doi.org/10.1177/1077546319889854.

[27] J. M. Londoño, S. A. Neild, J. E. Cooper, Identification of backbone curves of nonlinear systems from resonance decay responses, Journal of Sound and Vibration 348 (2015) 224–238. doi:https://doi.org/10.1016/j.jsv.2015.03.015.

[28] C. Stephan, H. Festjens, F. Renaud, J.-L. Dion, Poles tracking of weakly nonlinear structures using a bayesian smoothing method, Mechanical Systems and Signal Processing 84 (2017) 136–151, recent advances in nonlinear system identification. doi:https://doi.org/10.1016/j.ymssp.2015.05.028.

[29] R. M. Lacayo, M. S. Allen, Updating structural models containing nonlinear Iwan joints using quasi-static modal analysis, Mechanical Systems and Signal Processing 118 (2019) 133–157. doi:https://doi.org/10.1016/j.ymssp.2018.08.034.

[30] J.-L. Dion, G. Chevallier, N. Peyret, Improvement of measurement techniques for damping induced by micro-sliding, Mechanical Systems and Signal Processing 34 (1-2) (2013) 106–115.

[31] S. L. Brunton, J. L. Proctor, J. N. Kutz, Discovering governing equations from data by sparse identification of nonlinear dynamical systems, Proceedings of the National Academy of Sciences 113 (15) (2016) 3932–3937. doi:10.1073/pnas.1517384113.
URL https://www.pnas.org/doi/abs/10.1073/pnas.1517384113

[32] M. Lin, C. Cheng, Z. Peng, X. Dong, Y. Qu, G. Meng, Nonlinear dynamical system identification using the sparse regression and separable least squares methods, Journal of Sound and Vibration 505 (2021) 116141. doi:https://doi.org/10.1016/j.jsv.2021.116141.
URL https://www.sciencedirect.com/science/article/pii/S0022460X21002133

[33] R. Fuentes, R. Nayek, P. Gardner, N. Dervilis, T. Rogers, K. Worden, E. Cross, Equation discovery for nonlinear dynamical systems: A bayesian viewpoint, Mechanical Systems and Signal Processing 154 (2021) 107528. doi:https://doi.org/10.1016/j.ymssp.2020.107528.
URL https://www.sciencedirect.com/science/article/pii/S0888327020309146

[34] R. Tibshirani, Regression Shrinkage and Selection Via the Lasso, Journal of the Royal Statistical Society: Series B (Methodological) 58 (1) (1996) 267–288. doi:10.1111/j.2517-6161.1996.tb02080.x.
URL https://doi.org/10.1111/j.2517-6161.1996.tb02080.x

[35] S. Marelli, B. Sudret, UQLab: a framework for uncertainty quantification in MATLAB, in: Proc. 2nd Int. Conf. on Vulnerability, Risk Analysis and Management (ICVRAM2014), Liverpool, United Kingdom, 2014, pp. 2554–2563.

[36] R. da S Raqueti, R. O. Teloli, S. da Silva, P. Bussetta, A. Cunha Jr, On the use of stochastic bouc–wen model for simulating viscoelastic internal variables from a finite element approximation of steady-rolling

tire, Journal of Vibration and Control 0 (0) (2023) 10775463221125038. `arXiv:https://doi.org/10.1177/10775463221125038`, `doi:10.1177/10775463221125038`.
URL https://doi.org/10.1177/10775463221125038

[37] T. Burton, On the amplitude decay of strongly non-linear damped oscillators, Journal of Sound and Vibration 87 (4) (1983) 535–541. `doi:https://doi.org/10.1016/0022-460X(83)90504-7`.
URL https://www.sciencedirect.com/science/article/pii/0022460X83905047

[38] M. Krack, J. Gross, Harmonic balance for nonlinear vibration problems, Vol. 1, Springer, 2019.

[39] M. Feldman, Non-linear system vibration analysis using hilbert transform–i. free vibration analysis method 'freevib', Mechanical Systems and Signal Processing 8 (2) (1994) 119–127. `doi:https://doi.org/10.1006/mssp.1994.1011`.
URL https://www.sciencedirect.com/science/article/pii/S0888327084710119

[40] P. L. Green, K. Worden, Bayesian and Markov chain Monte Carlo methods for identifying nonlinear systems in the presence of uncertainty, Philosophical Transactions of the Royal Society A: Mathematical, Physical and Engineering Sciences 373 (2051) (2015) 20140405. `doi:http://doi.org/10.1098/rsta.2014.0405`.

[41] N. Peyret, J.-L. Dion, G. Chevallier, A framework for backbone experimental tracking: Piezoelectric actuators, stop-sine signal and kalman filtering, Mechanical Systems and Signal Processing 78 (2016) 28–42.

[42] H. N. E., S. Zheng, L. S. R., W. M. C., S. H. H., Z. Quanan, Y. Nai-Chyuan, T. C. Chao, L. H. H., The empirical mode decomposition and the Hilbert spectrum for nonlinear and non-stationary time series analysis, in: Proceedings of the Royal Society of London A, Vol. 454, The Royal Society, 1998, pp. 903–995.